RESEARCH ARTICLE | APRIL 27 2026

Ablation loading efficiency of carbon nanostructured foams produced with the pulsed laser deposition technique

M. Cipriani ✉ ; A. Maffini ; D. Orecchia ; M. S. Galli De Magistris ; V. Ciardiello ; M. Scisciò;
P. Andreoli; G. Cristofari ; E. Di Ferdinando; V. P. Loschiavo ; D. Davino ; M. Passoni; F. Consoli

Matter Radiat. Extremes 11, 047402 (2026)
https://doi.org/10.1063/5.0316156

Matter and
Radiation at Extremes

RESEARCH ARTICLE

pubs.aip.org/aip/mre

Ablation loading efficiency of carbon nanostructured foams produced with the pulsed laser deposition technique

Cite as: Matter Radiat. Extremes 11, 047402 (2026); doi: 10.1063/5.0316156
Submitted: 11 December 2025 • Accepted: 7 April 2026 •
Published Online: 27 April 2026

M. Cipriani,[1,a)] A. Maffini,[2] D. Orecchia,[2] M. S. Galli De Magistris,[2] V. Ciardiello,[3] M. Scisciò,[1] P. Andreoli,[1] G. Cristofari,[1] E. Di Ferdinando,[1] V. P. Loschiavo,[3] D. Davino,[3] M. Passoni,[2] and F. Consoli[1]

AFFILIATIONS

[1] ENEA, Nuclear Department, C.R. Frascati, Frascati, Italy
[2] Department of Energy, Politecnico di Milano, Milan, Italy
[3] Department of Engineering, University of Sannio, Benevento, Italy

[a)] **Author to whom correspondence should be addressed:** mattia.cipriani@enea.it

ABSTRACT

Porous materials have particular advantages for a variety of applications in inertial confinement fusion. To identify suitable new materials for these applications, it is important to investigate their interaction with high-power lasers and the associated plasma evolution. In this work, we report on the results of an experimental campaign performed at the ABC laser facility, employing carefully characterized nanostructured carbon foams obtained with the pulsed laser deposition technique. The enhancement of the ablation loading due to the foam buffer is evaluated by comparing the volume of the crater left after the interaction among different samples. Particular foam parameters and morphology are found to increase the ablation loading by producing a larger crater volume. Visible side-on streak camera images confirm these results. The absorption efficiency is investigated by time-resolved measurement of the laser light collected by focusing lenses and acquired by two fast photodiodes.

I. INTRODUCTION

Porous materials, or foams, are attracting much interest owing their wide range of potential applications. Foams have been used for increasing shock wave pressures,[1] for equation-of-state studies,[2] and for simulating plasma dynamics in laboratory astrophysics experiments,[3] and foams of near-critical density have been used as targets to drive effective direct laser acceleration of electrons[4] and thereby generate gamma and neutron sources.[5] In the context of inertial confinement fusion (ICF), the use of foams has been proposed to increase laser absorption,[6,7] to smooth spatial inhomogeneities in the energy profile of the laser beam,[8] to reduce the impact of laser–plasma instabilities (LPIs),[9,10] and to reproduce the long plasma of the capsule corona in shock-ignition schemes.[11] Recently, the idea of using foam as a support structure for liquid nuclear fuel[12] has been revived along with new ignition schemes.[13]

In general, foams have been made of plastic or silica, produced through chemical methods[14] or recently through 3D printing.[15] However, new materials and new manufacturing technologies must be explored to find the best material for every application. Mid-Z materials may be applied as ablators in direct-drive implosions, on the basis of their potential ability to mitigate the detrimental effects of two-plasmon decay instability.[16] A foam made of mid-Z materials may be a suitable candidate for an ablator for direct-drive ICF, potentially combining the mitigation of LPIs with a higher absorption efficiency and an increased ablation pressure on the following capsule layer. Pure carbon foams consisting of aggregates of nanoparticles can be produced through pulsed laser deposition (PLD). PLD is a physical vapor deposition technique that exploits a pulsed laser to remove material from a target inside a vacuum chamber. The ablated species travel in a controlled background atmosphere and are deposited on a substrate, resulting in the growth of a film.[17–19] If the working gas pressure is low, the ablated species can travel freely, arriving at the substrate with a sufficiently high energy to form a compact film. Conversely, high background pressures promote a progressive slowing-down process, up to a diffusive regime. Under these conditions, the ejected species can aggregate while in flight, producing a porous, nanostructured low-density film (i.e., a nanofoam).[20–22]

Carbon nanofoams produced by PLD have already been investigated both theoretically and experimentally for several applications related to laser–matter interaction with relativistic intensity ($I \geq 10^{18}$ W/cm^2) and ultrashort pulses ($\tau < 1$ ps), such as laser-driven particle acceleration and generation of secondary radiation. In these contexts, the controlled density and morphology of PLD carbon nanofoams have been exploited to tailor laser energy conversion into kinetic energy of electrons,[23] which, in turn, drives the generation of high-energy photons,[24,25] the acceleration of light ions via target normal sheath acceleration (TNSA),[26–28] and eventually the production of secondary products such as neutrons,[29] positrons,[30] and medical radioisotopes.[31]

Despite the considerable research effort devoted to the study of nanofoams in the context of interaction with high-intensity ultrashort lasers, the investigation of potential applications of carbon nanofoams for laser-driven ICF is still at a very early stage,[32] and substantial experimental and modeling work is needed to assess their viability and to refine suitable target configurations.

In this work, we present the results of an experimental campaign devoted to the direct laser irradiation at high power of pure carbon nanofoams manufactured through PLD at the Politecnico di Milano laboratories, with the main purpose of exploring their potential benefits when used as absorbers for fusion targets. The experiments were conducted at the ABC laser facility at ENEA Research Center in Frascati, in which the ABC main beam was employed at a wavelength of 1054 nm and at an intensity of 10^{14} W/cm^2, which is in the range of relevance for ICF studies. In fact, the typical intensities used for ICF research are of the same order of magnitude, especially in direct drive experiments,[33–35] where foams could be used as ablators, as discussed above. While the second or third harmonics of the Nd:glass laser are considered for ICF, we chose to work with the fundamental harmonic at 1054 nm, to maximize the laser energy on the target and thus to reach the highest possible intensities with a large focal spot diameter, increasing the ablation pressure in the plasma.

The main purpose of the campaign was to investigate the potential benefits of such advanced materials to explore their potential application as absorbers for fusion targets. Several effects will need to be studied for full-scale implosions, such as cross-beam energy transfer or LPIs, but simple planar experiments allow quick and easy investigation of fundamental properties of the interaction, such as the ablation loading, that then justify further investigation at larger and more complex facilities.

II. TARGETS

The nanostructured foams investigated in this work were manufactured through PLD deposition, which was performed using the second harmonic ($\lambda = 532$ nm) of a Q-switched Nd:YAG laser, characterized by a pulse duration of about 5–7 ns, operating at a repetition rate of 10 Hz with a pulse energy of 500 mJ. The laser was focused on a pyrolytic graphite target with an incidence angle of 45°. The distance between the target and the substrate was fixed at 70 mm, and the substrate holder rotated at 11 rpm to ensure a satisfactory thickness uniformity. The vacuum chamber was filled with argon gas (99.9% purity), with its pressure tuned to produce carbon nanostructured films with different densities and morphologies. Specifically, low-density foams (6 mg/cm^3) characterized by a fractal-like morphology were obtained at a pressure of 200 Pa, as shown in Figs. 1(a) and 1(c). Decreasing the Ar pressure to 50 Pa allowed the production of higher-density foams (26 mg/cm^3), featuring a tree-like morphology as depicted in Figs. 1(b) and 1(d). In the following, we will refer to these two categories of samples as *fractal-like foam* and *tree-like foam*, respectively. The mass thickness, defined as the product (average density) × (geometrical thickness) and also known as the areal density, was controlled by adjusting the deposition time, and it ranged from 0.08 to 0.16 mg/cm^2. In the case of fractal-like foams, this is equivalent to a foam thickness of ~133 and 267 μm, respectively, which decreases to ~30 and 60 μm for tree-like foams. Foams of the same mass thickness but different morphology (i.e., fractal-like or tree-like) were investigated to meaningfully compare targets with different densities under the same irradiation conditions. The mass thickness characterizations of the foam layers were performed through energy-dispersive X-ray spectroscopy (EDXS) coupled with the EDDIE MATLAB code,[36] allowing the retrieval of mass thickness data from EDXS spectra on the basis of a theoretical model of electron transport and characteristic X-ray emission. The geometrical thickness of the foams can be obtained through cross-sectional scanning electron microscope (SEM) images, and thus the foam density is determined by the mass thickness/geometrical thickness ratio. This approach can overcome the difficulties related to mass thickness and density measurements of such porous materials, and has been successfully applied for the characterization of PLD-produced nanofoams in multiple studies.[21,22,32]

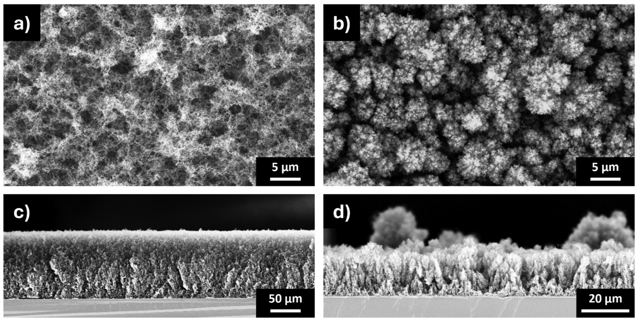

FIG. 1. Scanning electron microscope (SEM) images in planar and cross-sectional views of PLD-deposited carbon foams: (a) and (c) low-density (6 mg/cm^3) fractal-like foam; (b) and (d) intermediate-density (26 mg/cm^3) tree-like foam.

The PLD technique requires a substrate to support the foam deposition. Two types of aluminum substrates were used: large aluminum disks, ~1 mm thick, and aluminum foils with a thickness of 1 μm. We list the targets used in the campaign in Table I. To simplify the identification of each target throughout the text, we have defined a target label for each case. The first set of targets, shown in

TABLE I. Summary of targets used in experiments.

Target label	Foam type	Substrate	Holder	Thickness (μm)	Density (mg/cm^3)	Mass thickness (mg/cm^2)
BareDisc	No foam	Al thick	Al disk	1300	2700	⋯
FracDisc	Fractal-like	Al thick	Al disk	267	6	0.16
TreeDisc	Tree-like	Al thick	Al disk	60	26	0.16
Frac16	Fractal-like	1 μm Al	C-shaped	267	6	0.16
Frac08	Fractal-like	1 μm Al	C-shaped	133	6	0.08
Tree16	Tree-like	1 μm Al	C-shaped	60	26	0.16
Tree08	Tree-like	1 μm Al	C-shaped	30	26	0.08

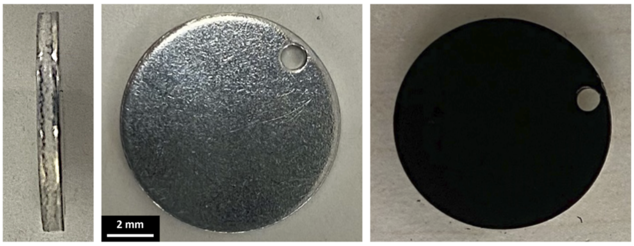

FIG. 2. Pictures of the aluminum disk substrate (a) before and (b) after foam deposition. The disk was 1 mm thick, with a diameter of 15 mm.

Fig. 2, was designed to estimate the potential increase in compression efficiency given by the foam buffer, by comparing the volume of the crater left on the substrate with and without the foam. We labeled the targets coated with the fractal-like and tree-like foams as "FracDisc" and "TreeDisc," respectively. The substrate was robust enough to not be destroyed during the interaction, allowing post-shot crater analysis. However, such a large target imposed some limitations on the plasma diagnostics, potentially casting a shadow on the streak camera looking at the side of the target (see Sec. III) and thus reducing the reliability of the laser-generated plasma imaging. To overcome this limitation and improve our understanding of plasma dynamics and interaction features, a second set of targets with 1 μm thick aluminum foils as substrates was prepared. The Al thickness was chosen as small as possible to reduce its influence on the overall evolution of the foam plasma, while still being strong enough to withstand the mechanical and thermal effects occurring during PLD deposition and target preparation. To support the aluminum foils and allow precise target alignment in the interaction chamber, the Al substrates were glued to 3D-printed C-shaped plastic frames, with a thickness of ~0.7 μm. A schematic representation of these targets is shown in Fig. 3. The C-shaped holder design, with a lateral aperture on one side of the frame, provided convenient access to both the front and rear sides of the target, useful for investigating the plasma evolution through the optical streak camera fielded in the campaign (see Sec. III). We labeled these targets by the foam morphology and the mass thickness: for example, "Frac16" refers to the fractal-like foam with a mass thickness of 0.16 mg/cm^2 coating the 1 μm aluminum substrate on the C-shaped holder.

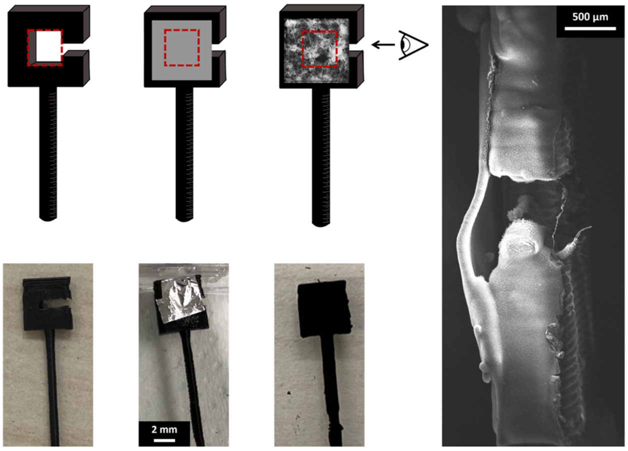

FIG. 3. Schematic illustration of the fabrication process of the foam samples on C-shaped holders (above), with corresponding real target pictures (below). On the right, a SEM image of the target in a lateral view is shown.

III. EXPERIMENTAL SETUP

The ABC laser at the ENEA Research Center in Frascati is a Nd:glass phosphate laser, which can deliver two counterpropagating beams of 100 J each at the fundamental wavelength $\lambda_L = 1054$ nm for a time duration of $\tau_L = 3$ ns. In this campaign, we used one of the two beams to irradiate the samples in a planar geometry at normal incidence. For all shots, the focal spot diameter was 100 μm and the energy was set to 40 J, for an intensity on target of 1.7×10^{14} W/cm^2.

A schematic illustration of the experimental setup is shown in Fig. 4. The light of the main beam is directed to the entrance of the experimental chamber by a pair of mirrors. A small leak from one of these is collected on photodiode L, as shown in Fig. 4, to record the time-resolved laser temporal profile. Photodiode L was calibrated using an absolutely calibrated calorimeter to obtain an immediate measure of the energy contained in the laser beam for each shot.

The light of the main beam is linearly polarized and passes through a polarizer unaltered. A $\lambda/4$ waveplate changes the polarization from linear to circular before the beam enters the experimental chamber. The circular polarization reduces the effect of absorption due to either p or s polarization, which would be significant with

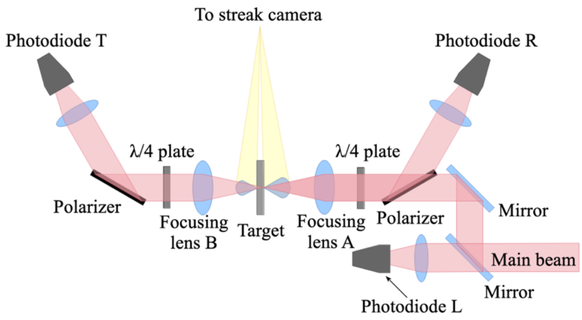

FIG. 4. Schematic of experimental setup.

a linear polarization of the main beam. (The absorption of the laser in the experiments was less affected by the angle of incidence and by the relative angle between the laser propagation direction and the density gradient of the laser-generated plasma.) Moreover, the circular polarization prevents the risk of backward reflections along the amplification chain, which would be destructive for the system. When the main beam hits the target, a portion of the laser light is reflected. The reflected light, which is still circularly polarized, passes again through the $\lambda/4$ waveplate, which transforms the polarization back to linear, but in a direction orthogonal to the original. The polarizer thus rejects the reflected light, protecting the laser amplification chain. In the experiments, this light was collected by photodiode R, to measure the fraction of light reflected from the target. In the same way, the transmitted light was collected by photodiode T on the other hand of the target, by exploiting the optics that are usually used for the second laser beam. Both of these photodiodes were calibrated relative to photodiode L.

A visible streak camera was used to image the plasma evolution at 90° from the laser axis. In the case of C-shaped targets, the streak camera was aligned with the lateral aperture of the support frame, to directly image the plasma. The magnification of the image on the streak camera slit was chosen to allow simultaneous imaging of both sides of the target. In this way, both the behavior of the plasma directly generated by the laser action and the plasma produced by the breakout of the shock wave from the aluminum substrate could be investigated.

IV. RESULTS

In this section, we present the results obtained during the irradiation of the targets listed in Table I.

A. Large disk substrates: Ablation loading efficiency

To evaluate the efficiency of the conversion of laser energy into ablation of the substrate, we measured the volume of the craters left on the thick aluminum disks after irradiation, comparing the results with and without the foam coating. This technique has been successfully adopted in other studies.[1,37] We employed a Leica DMI5000 M inverted microscope, equipped with the LAS Montage module, with a resolution of about 1 μm in depth to measure the crater volumes. The process of crater creation involves several physical mechanisms. The shock wave driven by the laser travels through the foam and reaches the surface of the substrate, leading to ablation and evaporation of the aluminum of the disk. It then propagates into the substrate, decaying along its depth. As the shock strength decays, the temperature behind the shock drops and eventually reaches the melting temperature. From this moment, the shock becomes an elastic wave, deforming the material but not melting or evaporating it. A detailed description of this process can be found, for example, in Refs. 37 and 38. Thus, an absolute measure of the crater volume should include an estimate of the influence of the melting and resolidification of the material after the action of the shock at low temperature. However, here, we are comparing the volumes between the different cases. Under the reasonable assumption that the processes of melting and resolidification has the same effect on the crater volume in all the cases, we can neglect the uncertainty related to these processes in the final stages of shock propagation.

In Fig. 5, we show 3D reconstructions of the craters obtained after shots on thick aluminum substrates. The calculated volumes

TABLE II. Crater diameters and volumes for the Disc targets.

Target	Crater diameter (μm)	Crater volume (μm^3)
BareDisc	500	3.4×10^7
FracDisc	550	4.0×10^7
TreeDisc	600	6.0×10^7

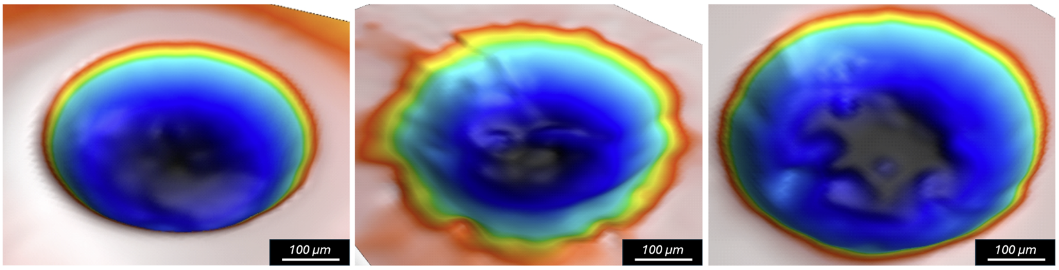

(a) (b) (c)

FIG. 5. 3D microscope reconstruction of craters left on Al substrate after laser interaction on targets with thick aluminum disks: (a) BareDisc; (b) FracDisc; (c) TreeDisc. The color scale indicates the depth in arbitrary units.

are reported in Table II. As can be seen, the crater left on the BareDisc in Fig. 5(a) has a distinct margin and a very smooth shape, which is directly related to the circular transverse profile of the laser beam. On the other hand, the crater left on the FracDisc [Fig. 5(b)] has a very irregular margins and is not symmetrical around its center. The volume of the crater as estimated from the microscope reconstruction is of the same order as the reference one (bare Al disk). We attribute this shape to the diffusion of laser light due to the fractal structure of the foam, which enlarges and deforms the final shape of the crater. To confirm this hypothesis, we prepared a special target with a thick fractal foam on a 100 nm plastic substrate, which indeed demonstrated a high foam transparency, as we discuss in Sec. IV B 2. Owing to the buffer transparency, the laser directly irradiated the substrate, leading to ablation conditions similar to those of the bare target, but with a wider crater.

Figure 5(c) shows the shape of the crater left after irradiation of the TreeDisc. The crater margin is more regular than that of the crater on the FracDisc in Fig. 5(b), and more similar to that of the crater on the BareDisc in Fig. 5(a). Furthermore, the volume of the crater is almost two times that of the crater on the bare disk, with only a moderately larger diameter. This indicates an increased efficiency in the ablation of the substrate due to the foam buffer. This relates to the low transparency of the tree-like foam used in this case compared with the fractal-like one, as discussed in Sec. IV B, which can also be associated with a low diffusion of the laser light in the foam. We attribute this enhancement of the ablation loading on the substrate to the higher absorption efficiency of the tree-like foam, compared with the fractal-like morphology.

We also obtained SEM images of the craters to provide further information on their micro- and nano-scale morphological features. From the micrographs in Fig. 6, it is possible to highlight some relevant features of the three types of targets. The crater on the BareDisc has a diameter of around 500 μm, is characterized by sharp walls, and shows some features at its bottom that are ascribable to resolidification of melted metal, as expected during the final stages of high-power laser–matter interaction. In the case of the FracDisc, the crater walls are much more irregular, and the resolidification features at the bottom of the crater are larger and more evident. The crater diameter is about 550 μm. These differences can be ascribed to the interaction of the laser pulse with the disordered foam structure, which breaks the symmetry of the laser front, potentially creating hotspots and promoting hydrodynamic instabilities in the melted metal. Finally, the TreeDisc shows a crater with the largest diameter of 600 μm. Interestingly, in this last case, the walls of the crater are quite sharp, although not as much as those on the BareDisc, and the resolidification features are even more

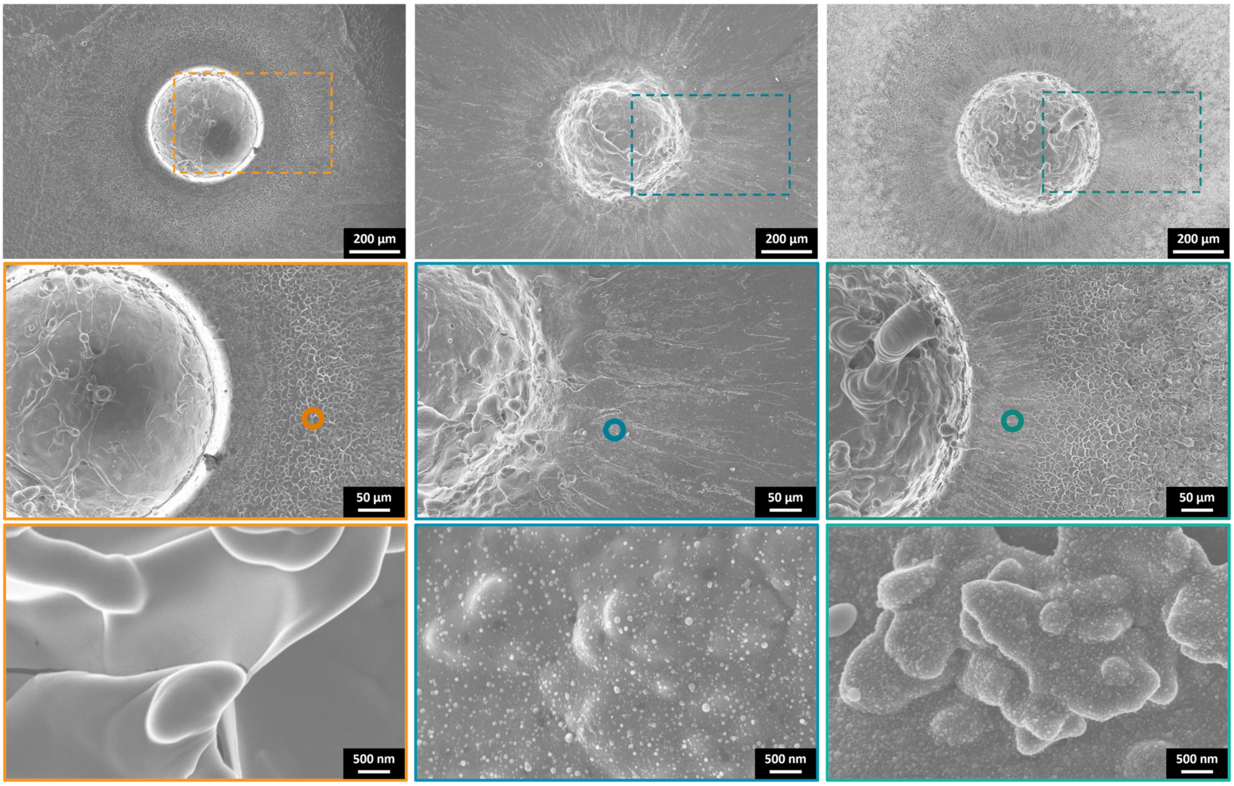

FIG. 6. SEM images of ablation craters formed on different targets: (a) BareDisc; (b) FracDisc; (c) TreeDisc. The middle row highlights the microscale structures around the crater edges. The bottom row shows higher-magnification images of the areas surrounding the craters, in the spots marked with circles in the middle row, highlighting the nanoscale features and the presence of nanoparticles.

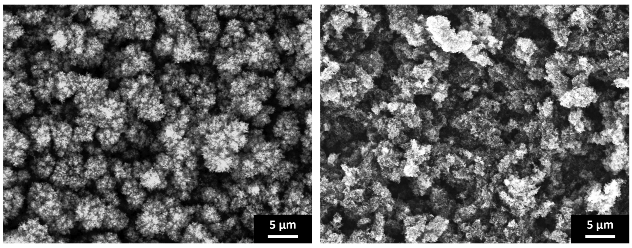

FIG. 7. SEM images of (a) the as-deposited tree-like foam and (b) as it looked like far from the crater after the shot.

predominant than in the fractal-like case. The larger crater, together with the sharp crater edges, is consistent with a significant enhancement of ablation loading due to the tree-like buffer, which at the same time limits the detrimental effects on pulse shape seen with the fractal-like target. These observations support the results obtained with the optical inverted microscope, and reveal further details of the laser–nanostructure interaction.

It is also interesting to comment on the morphological modification of the area surrounding the ablation craters. A circular region is visible close to the edge, featuring cracks and fissures, probably a consequence of the stresses and high temperatures induced in the material after laser interaction. The structures in this area are similar for the BAREDISC and TREEDISC, while they are absent for the FRACDISC. Instead, the whole region surrounding the FRACDISC crater is characterized by jets of resolidified melt material, which are also present at the crater edge in the TREEDISC case. Their large extension for the fractal-like foam buffer can be associated with the rough crater edges and attributed to ejection and deposition of the melted material in the surrounding area. Going outward from the crater, a gradual transition region can be observed. Here, increasingly thick foam residues can be observed for both the FRACDISC and TREEDISC samples. In the outer portions of the target, most of the foam is still present, although it presents a partially altered morphology (see Fig. 7), likely due to the mechanical stresses, vibrations, and thermal effects resulting from the laser-generated shock wave. We can also identify nanoparticles in the regions surrounding the craters of all the foam targets, being absent in the case of bare aluminum. These nanoparticles, likely originating from the foam

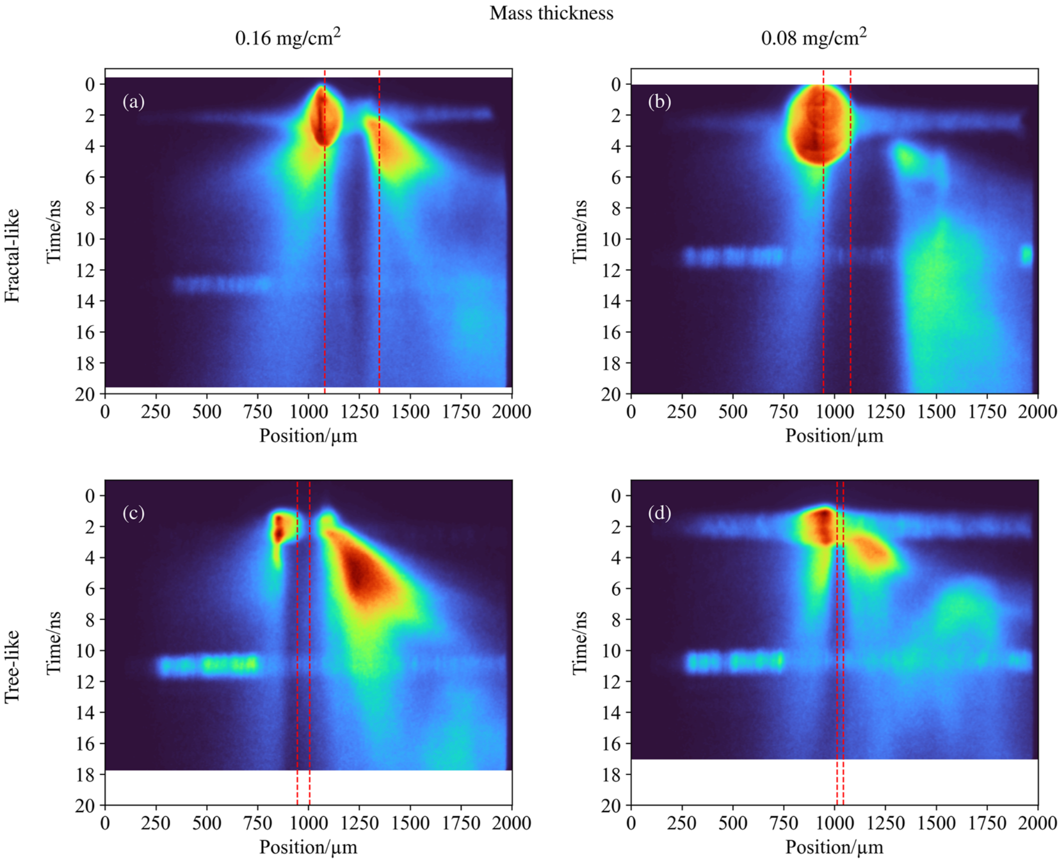

FIG. 8. Visible streak images for the four shots with a foam buffer on thin aluminum substrates. The mass thickness of the foam and its morphology are indicated at the top and on the left of the images, respectively. The origin of the y axis has been set at the instant of arrival of the main beam on the target. The red dashed vertical lines indicate the original position of the target (substrate + foam buffer). The laser is coming from the left.

layer itself and possibly redeposited after laser–matter interaction, are more densely distributed on the TreeDisc than the FracDisc (see Fig. 6), consistently with the morphology of the two buffers, which were more compact and more porous, respectively.

B. Thin substrates

To obtain detailed information on the laser-generated plasma, we employed thin aluminum substrates mounted on C-shaped supports. The visible streak camera and the photodiodes for reflected and transmitted light, shown in Fig. 4, provided information on plasma evolution.

1. Visible streak camera

Figure 8 shows the results of the shots with the thin aluminum substrate indicated in Table I. In the images, the laser is coming from the left and the vertical red dashed lines correspond to the approximate original position of the target. A green probe beam was used as a fiducial for the streaked images and is visible as the horizontal bright line at 12 ns in Fig. 8(a) and at 10 ns in all other images of Fig. 8. The probe beam was generated from a pick-up of the main beam itself along the amplification line and was therefore absolutely synchronized with the main beam.

At the beginning of the interaction, the main beam ablates the target, thus generating a plasma plume that expands toward the laser, visible in the images through its self-emission on the left of the initial target position. At the same time, a shock wave is generated into the material, which propagates in the same direction as the laser and eventually reaches the rear side of the target, generating the self-emission visible on the right of the initial target position.

The total power for the plasma self-emission follows the formula

$$W \propto \sqrt{T} Z^3 \rho, \qquad (1)$$

where T is the plasma temperature, Z is the ionization degree and ρ is the density. Assuming that Z did not vary appreciably across the dataset at the beginning of the ejection of the plasma from the rear side, the same self-emission can be obtained either with a cold and dense plasma or with a hot, although less dense, plasma. The self-emission in the Tree16 case was the most extended in time among all the cases, and it had the highest intensity, meaning that a large total mass of material was ejected after the shock breakout. The Frac16 target, in Fig. 8(a), shows a less evident rear-side plasma compared with Fig. 8(c). The rear-side plasma is less visible in the Tree08 case, in Fig. 8(d), while in the case of the Frac08 target, in Fig. 8(b), the plasma emitted from the back side of the target is barely visible. In all cases but Tree16, we also expect that the ejected plasma temperature was increased by the heating due to the transmitted laser light [see Fig. 9(b)], which then increased the plasma self-emission, according to Eq. (1). These results indicate that with the Tree16 target, we obtained the largest amount of ejected mass at shock breakout and thus the highest ablation pressure, confirming the conclusions already drawn from the crater results.

Quantitatively, we can strengthen these observations by considering the plasma expansion velocity at the rear side. To measure the plasma expansion velocity, we traced lineouts in the rear region and identified the time of rise of the self-emitted light. Owing to the spurious light recorded by the streak camera during the irradiation by the laser, we obtained quite large errors on this measurement. The largest velocity of 150 ± 20 km/s was obtained in the case of Frac08, while we obtained 130 ± 20 km/s for Tree16, 110 ± 20 km/s for Frac16, and 100 ± 40 km/s in the case of Tree08. However, we must consider that for Frac08, we obtained the largest integral of the transmitted light, as discussed in Sec. IV B 2. A large transmission of the laser light reasonably increased the ejected plasma temperature, and then its pressure and thus its expansion velocity. The same consideration holds for the Frac16 and Tree08 targets, where a degree of transmitted light was observed [see Fig. 9(b)]. In the Tree16 case, however, no transmitted light was recorded, but the expansion velocity of the plasma was the second largest, thus indicating a larger ablation pressure.

The analysis of the streak camera images thus confirms the conclusions of the crater investigation, discussed in Sec. IV A. The most evident plasma self-emission on the rear of the target corresponds to the Tree16 sample, suggesting a higher ablation pressure, in accordance with the larger crater volume obtained with the corresponding disk substrate. This case can be compared directly with the Frac16 case, having the same mass thickness, but showing a less-intense plasma with a shorter lifetime. This can be interpreted as a lower total mass of the emitted plasma at the target rear side, and thus as a

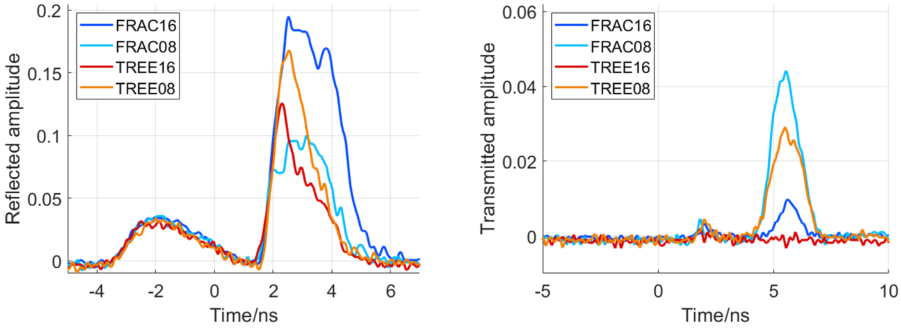

(a) (b)

FIG. 9. Normalized (a) reflected and (b) transmitted light for the shots on the thin aluminum substrate targets. The first peak at the beginning of the signals in (a) comes from a partial reflection from the chamber window and has been used as a fiducial for synchronization.

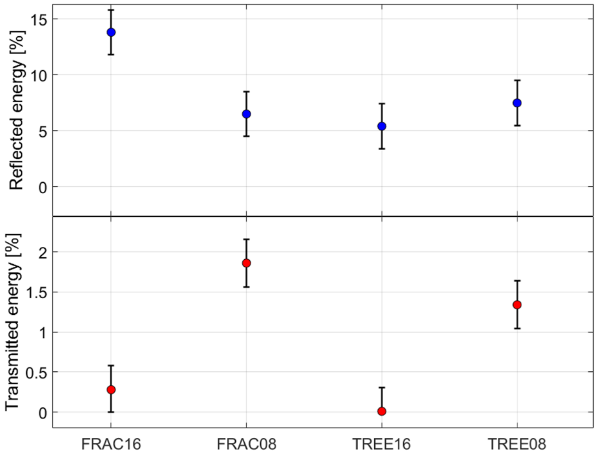

FIG. 10. Time-integral values of the signals in Figs. 9(a) and 9(b), normalized to the integral of the corresponding signal from photodiode L, which is proportional to the total laser energy.

lower ablation pressure, compared with the thick tree-like foam. The two other cases follow the same trend, but with a generally lower rear-side plasma self-emission, consistent with the reduced foam buffer mass thickness.

2. Absorption efficiency

Measurement of the laser light reflected by the target, or transmitted through it, provides an indication of the absorption efficiency of the material. As described in Sec. III, both reflected and transmitted laser light were collected by the focusing optics of the two main beams of the ABC facility and sent to two photodiodes for detection. The collection efficiency of the focusing optics is estimated to be 80%.[6] Figures 9(a) and 9(b) show the signals from photodiodes R and L, respectively, for each kind of target, normalized to the maximum amplitude of the signal from photodiode L. This allows us to compare them regardless of the slight variation in laser energy between shots. The time integrals of these signals are shown in Fig. 10 and have been normalized to the integral of the signal from photodiode L for each shot. The error has been estimated considering the noise on the amplitude of the signals from all the photodiodes, the time uncertainty due to the sampling rate of the oscilloscopes on which they have been acquired, and the potential effect of the laser–matter-generated electromagnetic pulses (EMPs), as done in Ref. 6.

The synchronization of the signals from photodiodes L, R, and T was achieved by the following procedure. The first peak in the curves from photodiode R in Fig. 9(a) comes from a reflection from the chamber window. We used this as a fiducial, and aligned the signal obtained from photodiode L with it. By accurate measurement of the optical paths of both the main beam and the reflected beam, we were able to determine the temporal delay between the main beam and the reflection from the chamber window in the signal on photodiode R, obtaining the desired synchronization between the main beam and the light reflected from the target. The signal from photodiode T was acquired on the same oscilloscope as photodiode R: these signals were automatically synchronized. By measuring the difference in length of the cables connecting the photodiodes to the oscilloscope, we calculated the time delay between the two signals, allowing precise synchronization.

Considering the FRAC16 and FRAC08 results, the amplitude of the reflected light signal was twice as high in the former than in the latter, with the time integral being more than twice as large. Moreover, the peak of the transmitted signal had an amplitude more than four times higher in the FRAC08 case than in the FRAC16 case. This can be related to the greater mass thickness of the foam buffer in the latter than in the former. More specifically, for the FRAC08 target, more light was transmitted through the foam and more energy reached the substrate, resulting in a faster ablation of the latter; this then led to earlier and higher laser transmission, owing to faster complete ablation of the target. On the other hand, in the FRAC16 case, the thicker foam survived longer, thus delaying the destruction of the substrate and therefore transmitting less laser energy. These effects have to be considered together with the information that the fractal-like foam, despite having an overcritical average density for the laser wavelength, proved to have a high transparency to the laser light. To this end, we exploited a test target consisting of a 100 nm-thick plastic substrate coated with a 267 μm-thick fractal-like foam buffer, all supported by an aluminum frame mounted on a glass rod. With this kind of target, the transmitted light was much more intense than in all the other cases, with a time duration comparable to that of the main beam, providing evidence of substantial foam transparency.

The picture is different when tree-like foams are considered. The amplitude of the reflected light signal for the TREE16 target was significantly lower than that for the FRAC16 case, with a much shorter time duration; moreover, no laser light transmission was detected, as can be seen in Fig. 9. These two factors indicate a substantially higher degree of absorption of the laser light into the tree-like foam buffer. The amplitude and time duration of the reflected light signal for the TREE08 case were intermediate between those for the FRAC16 and the TREE16 cases. Considering on the other hand the transmitted light signals, we see that the amplitude for the TREE08 case was close to but lower than that for the FRAC08 case. A coherent picture can be drawn by combining these data with the results of the crater measurement on the Al disks described in Sec. IV A. When fractal-like foams are used, a significant fraction of the laser light can pass through the foam without significant interaction and reach the substrate from the beginning. Therefore, the fraction of laser energy deposited in the foam that contributes to building up the pressure in the plasma is lower than in the case of tree-like foams, for which the transparency is low for 30 μm thickness (TREE08) and zero for 60 μm thickness (TREE16). In the latter case, the fraction of reflected light is also small, indicating a high absorption efficiency that contributes to an efficient pressure buildup, leading to a high ablation efficiency, as indicated by the crater volume analysis. These effects can be interpreted by considering that the laser wavelength λ is much larger than the radius a of the nanoparticles. According to the Mie theory of scattering,[39] the interaction of the laser light impinging on the nanoparticles undergoes two effects: absorption and scattering. The amount of light remaining after each nanoparticle along the propagation direction is given by the extinction efficiency factor Q_{ext} which is connected to the absorption efficiency factor Q_{abs} and to the scattering efficiency factor Q_{sca} through the relation $Q_{ext} = Q_{abs} + Q_{sca}$. The expression for Q_{ext} in our case $a \ll \lambda$ is (see, e.g., Ref. 39)

$$Q_{ext} \propto x \operatorname{Im}\left(\frac{m^2 - 1}{m^2 + 2}\right), \quad (2)$$

where $x = a/\lambda$ and m is the complex refractive index of carbon. Therefore, the amount of transmitted light is very large in our case when a single sphere is considered. On the other hand, in the experiments, the actual interaction of the laser with the foam was realized on aggregates rather than on single nanoparticles. The detailed description of this problem is complex, and we leave it to a subsequent paper. However, we can explain the relative difference in transmittance between fractal- and tree-like foams by the following argument. The thickness of the aggregates in fractal-like foams is of a similar order to the size of the nanoparticle, and they are more sparse in the foam volume compared with the tree-like ones. Therefore, we can expect that the extinction efficiency of an aggregate is not very different from that of a single particle. In tree-like foams, the aggregates are much thicker, and in this case the extinction factor is much larger, indicating a stronger absorption. This explains the larger transmitted light signal for fractal-like foams compared with tree-like foams, even with the same mass thickness.

V. CONCLUSIONS

We have reported here the results of an experimental campaign conducted at the ABC laser facility at the ENEA Research Center in Frascati with carbon nanofoams produced by PLD at the laboratories of the Politecnico di Milano. Two different morphologies of carbon foams were produced: fractal-like and tree-like. Samples were irradiated with an intensity of about 10^{14} W/cm^2 at the fundamental laser wavelength of the ABC laser. The fractal-like and tree-like foams had densities of 6 and 26 mg/cm^3, respectively. Two mass thicknesses were chosen to compare the performances of the two morphologies under irradiation, with the amount of matter facing the laser kept constant. Foams with both of these morphologies were deposited on thick disks and thin foils of aluminum. The former were exploited for measuring the ablation crater left after the interaction, while the latter were used to study the plasma behavior more accurately. An inverted optical microscope and an SEM were used to analyze the craters after irradiation, measuring the crater volume and its micro- and nanoscale features. With the targets on thin foil substrates, a visible streak camera was employed to evaluate the spatial extension of the plasma from the irradiated and the non-irradiated sides of the target. Two fast photodiodes were used to collect the laser light reflected by and transmitted through the target, to investigate the absorption of the laser in the foam buffers.

The crater analysis revealed that the tree-like foam is capable of increasing the ablation loading compared with irradiation of the bare substrate; in fact, the volume of the crater in the former case was twice as large as the latter. The edges of the crater were almost as sharp as in the bare case. On the other hand, the fractal-like foam, probably because of its large transparency, produced a crater of the same volume as in the bare case, with blurred edges, probably because of diffusion and scattering of laser light. The streak images support this conclusion, indicating a sustained plasma emission from the non-irradiated side of the target in the case of the tree-like foam coating. For the fractal-like foam targets, instead, this emission was less evident, and the spatial extension of the plasma on the irradiated side was larger than in the tree-like case, indicating a higher transparency. Measurements of reflected and transmitted light revealed a better absorption performance of the tree-like foam compared with the fractal-like foam. To increase the accuracy of measurements of the reflected, transmitted, and scattered light, we plan to field in the future experiments tailored optical fibers to collect the light diffused outside the solid angle covered by the focusing optics.

The results of this work indicate that tree-like foams are promising materials for increasing laser absorption and compression in inertial fusion studies. Future developments of this work will concern the theoretical modeling of the interaction in this experimental setting, as the nanometer-scale features in the internal structure of these foams require dedicated modeling approaches. Moreover, we will exploit the capabilities of the PLD technique, looking for new morphologies and structural features for new targets to be irradiated in the near future at the ABC facility.

ACKNOWLEDGMENTS

The authors thank A. Moriani at ENEA–Research Center Frascati for his support in analyzing the craters in Fig. 5. This work has been carried out within the framework of the EUROfusion Consortium, funded by the European Union via the Euratom Research and Training Programme (Grant Agreement No. 101052200–EUROfusion). Views and opinions expressed are, however, those of the authors only and do not necessarily reflect those of the European Union or the European Commission. Neither the European Union nor the European Commission can be held responsible for them. The authors also acknowledge the financial support of the European Union Next Generation EU and Italian Ministry of University and Research as part of the PRIN 2022 program, project "Nanomaterials for Fusion: Experimental and Modeling of Nanostructured Materials and Plasma–Material Interactions for Inertial and Magnetic Confinement Fusion" (Project ID: 2022N5JBHT, CUP D53D23002840006).

AUTHOR DECLARATIONS

Conflict of Interest

The authors have no conflicts to disclose.

Author Contributions

M. Cipriani: Conceptualization (equal); Data curation (equal); Formal analysis (equal); Investigation (equal); Visualization (equal); Writing – original draft (lead); Writing – review & editing (equal). **A. Maffini**: Conceptualization (equal); Formal analysis (equal); Investigation (equal); Visualization (equal); Writing – review & editing (equal). **D. Orecchia**: Conceptualization (equal); Formal analysis (equal); Investigation (equal); Visualization (equal); Writing – review & editing (equal). **M. S. Galli De Magistris**: Conceptualization (equal); Formal analysis (equal); Investigation (equal); Visualization (equal); Writing – review & editing (equal). **V. Ciardiello**: Conceptualization (equal); Formal analysis (equal); Investigation (equal); Visualization (equal); Writing – review & editing (equal). **M. Scisciò**: Conceptualization (equal); Formal analysis (equal); Investigation (equal); Visualization (equal); Writing – review & editing (equal). **P. Andreoli**: Conceptualization (equal); Data curation (equal); Investigation (equal). **G. Cristofari**: Data curation (equal); Investigation (equal). **E. Di Ferdinando**: Data curation (equal); Investigation (equal). **V. P. Loschiavo**: Conceptualization (equal); Formal analysis (equal); Investigation (equal); Visualization (equal); Writing – review & editing (equal). **D. Davino**: Conceptualization (equal); Formal analysis (equal); Investigation (equal); Visualization (equal); Writing – review & editing (equal). **M. Passoni**: Conceptualization (equal); Investigation (equal); Writing – review & editing (equal). **F. Consoli**: Conceptualization (equal); Investigation (equal); Writing – review & editing (equal).

DATA AVAILABILITY

The data that support the findings of this study are available from the corresponding author upon reasonable request.

REFERENCES

[1] R. De Angelis, F. Consoli, S. Yu. Gus'kov, A. A. Rupasov, P. Andreoli *et al.*, "Laser-ablated loading of solid target through foams of overcritical density," Phys. Plasmas **22**, 072701 (2015).

[2] A. Benuzzi-Mounaix, M. Koenig, G. Huser, B. Faral, D. Batani *et al.*, "Absolute equation of state measurements of iron using laser driven shocks," Phys. Plasmas **9**, 2466–2469 (2002).

[3] G. Rigon, B. Albertazzi, T. Pikuz, P. Mabey, V. Bouffetier *et al.*, "Micron-scale phenomena observed in a turbulent laser-produced plasma," Nat. Commun. **12**, 2679 (2021).

[4] O. N. Rosmej, M. Gyrdymov, N. E. Andreev, P. Tavana, V. Popov *et al.*, "Advanced plasma target from pre-ionized low-density foam for effective and robust direct laser acceleration of electrons," High Power Laser Sci. Eng. **13**, e3 (2025).

[5] M. M. Günther, O. N. Rosmej, P. Tavana, M. Gyrdymov, A. Skobliakov *et al.*, "Forward-looking insights in laser-generated ultra-intense γ-ray and neutron sources for nuclear application and science," Nat. Commun. **13**, 170 (2022).

[6] M. Cipriani, S. Y. Gus'kov, F. Consoli, R. De Angelis, A. A. Rupasov *et al.*, "Time-dependent measurement of high-power laser light reflection by low-Z foam plasma," High Power Laser Sci. Eng. **9**, e40 (2021).

[7] A. É. Bugrov, S. Yu. Gus'kov, V. B. Rozanov, I. N. Burdonskii, V. V. Gavrilov *et al.*, "Absorption and scattering of high-power laser radiation in low-density porous media," J. Exp. Theor. Phys. **88**, 441–448 (1999).

[8] S. Depierreux, C. Labaune, D. T. Michel, C. Stenz, P. Nicolaï *et al.*, "Laser smoothing and imprint reduction with a foam layer in the multikilojoule regime," Phys. Rev. Lett. **102**, 195005 (2009).

[9] D. A. Mariscal, O. S. Jones, R. L. Berger, S. Patankar, K. L. Baker *et al.*, "Laser transport and backscatter in low-density SiO_2 and Ta_2O_5 foams," Phys. Plasmas **28**, 013106 (2021).

[10] L. Hudec, J. Limpouch, O. Renner, V. T. Tikhonchuk, R. Dudzak *et al.*, "Investigation of ion temperature in low-density undercritical foams," Plasma Phys. Controlled Fusion **67**, 025022 (2025).

[11] V. T. Tikhonchuk and S. Weber, "Physics of porous materials under extreme laser-generated conditions," Matter Radiat. Extremes **9**, 033001 (2024).

[12] R. A. Sacks and D. H. Darling, "Direct drive cryogenic ICF capsules employing D-T wetted foam," Nucl. Fusion **27**, 447–452 (1987).

[13] I. V. Igumenshchev, W. Theobald, C. Stoeckl, R. C. Shah, D. T. Bishel *et al.*, "Proof-of-principle experiment on the dynamic shell formation for inertial confinement fusion," Phys. Rev. Lett. **131**, 015102 (2023).

[14] K. Nagai, C. S. A. Musgrave, and W. Nazarov, "A review of low density porous materials used in laser plasma experiments," Phys. Plasmas **25**, 030501 (2018).

[15] T. Wiste, O. Maliuk, V. Tikhonchuk, T. Lastovicka, J. Homola *et al.*, "Additive manufactured foam targets for experiments on high-power laser–matter interaction," J. Appl. Phys. **133**, 043101 (2023).

[16] M. Lafon, R. Betti, K. S. Anderson, T. J. B. Collins, R. Epstein *et al.*, "Direct-drive–ignition designs with mid-Z ablators," Phys. Plasmas **22**, 032703 (2015).

[17] D. B. Chrisey and G. Hubler, *Pulsed Laser Deposition* (NRL Review, 1994).

[18] H.-U. Krebs, M. Weisheit, J. Faupel, E. Süske, T. Scharf *et al.*, "Pulsed laser deposition (PLD)—A versatile thin film technique," in *Advances in Solid State Physics* (Springer, 2003), pp. 505–518.

[19] M. N. R. Ashfold, F. Claeyssens, G. M. Fuge, and S. J. Henley, "Pulsed laser ablation and deposition of thin films," Chem. Soc. Rev. **33**, 23–31 (2004).

[20] A. Maffini, A. Pazzaglia, D. Dellasega, V. Russo, and M. Passoni, "Growth dynamics of pulsed laser deposited nanofoams," Phys. Rev. Mater. **3**, 083404 (2019).

[21] A. Maffini, D. Orecchia, A. Pazzaglia, M. Zavelani-Rossi, and M. Passoni, "Pulsed laser deposition of carbon nanofoam," Appl. Surf. Sci. **599**, 153859 (2022).

[22] D. Orecchia, A. Maffini, M. Zavelani-Rossi, and M. Passoni, "Versatile synthesis of nanofoams through femtosecond pulsed laser deposition," Small Struct. **5**, 2300560 (2024).

[23] A. Pazzaglia, L. Fedeli, A. Formenti, A. Maffini, and M. Passoni, "A theoretical model of laser-driven ion acceleration from near-critical double-layer targets," Commun. Phys. **3**, 133 (2020).

[24] M. Galbiati, A. Formenti, M. Grech, and M. Passoni, "Numerical investigation of non-linear inverse Compton scattering in double-layer targets," Front. Phys. **11**, 1117543 (2023).

[25] A. Formenti, M. Galbiati, and M. Passoni, "Three-dimensional particle-in-cell simulations of laser-driven multiradiation sources based on double-layer targets," Phys. Rev. E **109**, 035206 (2024).

[26] I. Prencipe, J. Metzkes-Ng, A. Pazzaglia, C. Bernert, D. Dellasega *et al.*, "Efficient laser-driven proton and Bremsstrahlung generation from cluster-assembled foam targets," New J. Phys. **23**, 093015 (2021).

[27] A. Maffini, F. Mirani, M. Galbiati, K. Ambrogioni, F. Gatti *et al.*, "Towards compact laser-driven accelerators: Exploring the potential of advanced double-layer targets," EPJ Tech. Instrum. **10**, 15 (2023).

[28] F. Mirani, K. Ambrogioni, A. Maffini, F. Gatti, M. S. Galli De Magistris *et al.*, "Addressing the role of advanced targets for enhanced control of laser-driven hadron sources," Phys. Rev. Appl. **24**, 014017 (2025).

[29] F. Mirani, A. Maffini, and M. Passoni, "Laser-driven neutron generation with near-critical targets and application to materials characterization," Phys. Rev. Appl. **19**, 044020 (2023).

[30] M. Galbiati, K. Ambrogioni, L. F. C. Monaco, M. S. Galli De Magistris, D. Orecchia *et al.*, "Numerical proof-of-concept of nanofoam-based targets for proton acceleration and high-energy photon and positron generation in strong fields," Sci. Rep. (submitted) (2025).

[31] A. Maffini, F. Mirani, A. C. Giovannelli, A. Formenti, and M. Passoni, "Laser-driven production with advanced targets of copper-64 for medical applications," Front. Phys. **11**, 1223023 (2023).

[32] A. Maffini, M. Cipriani, D. Orecchia, V. Ciardiello, A. Formenti *et al.*, "Numerical study of carbon nanofoam targets for laser-driven inertial fusion experiments," Laser Part. Beams **2023**, e1.

[33] R. S. Craxton, K. S. Anderson, T. R. Boehly, V. N. Goncharov, D. R. Harding *et al.*, "Direct-drive inertial confinement fusion: A review," Phys. Plasmas **22**, 110501 (2015).

[34] E. M. Campbell, T. C. Sangster, V. N. Goncharov, J. D. Zuegel, S. F. B. Morse *et al.*, "Direct-drive laser fusion: Status, plans and future," Philos. Trans. R. Soc. A **379**, 20200011 (2021).

[35] O. A. Hurricane, P. K. Patel, R. Betti, D. H. Froula, S. P. Regan *et al.*, "Physics principles of inertial confinement fusion and U.S. program overview," Rev. Mod. Phys. **95**, 025005 (2023).

[36] A. Pazzaglia, A. Maffini, D. Dellasega, A. Lamperti, and M. Passoni, "Reference-free evaluation of thin films mass thickness and composition

through energy dispersive x-ray spectroscopy," Mater. Charact. **153**, 92–102 (2019).

[37] E. A. Bolkhovitinov, B. L. Vasin, S. Y. Gus'kov, I. Ya. Doskach, A. A. Erokhin *et al.*, "Crater formation in a target under the action of a high-power laser pulse," Plasma Phys. Rep. **30**, 183–186 (2004).

[38] K. S. Gus'kov and S. Y. Gus'kov, "Efficiency of ablation loading and the limiting destruction depth of material irradiated by a high-power laser pulse," Quantum Electron. **31**, 305–310 (2001).

[39] H. C. van de Hulst, *Light Scattering by Small Particles* (Dover Publications, New York, 1981).